Comparing the Luttinger–Kohn–Pikus–Bir and the Empiric K·P Hamiltonians in quantum dot intermediate band solar cells manufactured in zincblende semiconductors

Antonio Luque , Aleksandr Panchak , Alex Mellor , Alexey Vlasov , Antonio Martí , Viacheslav Andreev

A B S T R A C T

The calculation of the energy spectrum and absorption coefficients of quantum dot nanostructured intermediate band solar cells using the Empiric K·P Hamiltonian method and its agreement with experimental data are summarized. The well established Luttinger Kohn Hamiltonian modified by Pikus and Bir for strained material, such as quantum dot arrays, is presented using a simplified strain field that allows for square band offsets. The energy spectrum and absorption coefficients are calculated with this new Hamiltonian. With the approximations made the energy spectrum results to be exactly the same but the absorption coefficient fits experiments less accurately. The computer time using the latter Hamiltonian is much longer than the former one.

1. Introduction

The intermediate band (IB) solar cells (SC) [1] include a band or set of levels situated in the bandgap of an ordinary semiconductor. These allow for sub-bandgap quantum efficiency using the IB as a stepping stone for electron–hole generation. IBs may be formed by the states of the conduction band electrons confined by quantum dots [2]. Much of the activity associated with this topic uses semiconductors with zincblende crystal structure.

For a sound understanding of the quantum dot (QD) IBSC operation, a model for the calculation of the light absorption mechanisms is very convenient. Simplicity of use and capacity of feedback with the device engineers is very desirable. The Empiric K·P Hamiltonian (EKPH) has been developed with this purpose [3,4].

The usual way of approaching this problem when using nanostructured zincblende materials is the use of the eight band Luttinger Kohn (LK) [5,6] Hamiltonian modified by Pikus and Bir (PB) [7,8] which accounts for the strain in the lattice. This is a variety of the K·P method introduced by Dresselhaus Kip and Kittel [9] and extensively developed by Kane [10,11] for calculations of semiconductor band structures.

However, in the used form, the EKPH method is much faster and easy to handle than the LK–PB Hamiltonian (LKPBH) method. The purpose of this paper is to compare the two methods.

Beyond this introduction, this paper is organized as follows. Section 2 summarizes the theoretical bases of the K·P methods. Section 3 describes the EKPH method leading to a 4-Band Hamiltonian matrix. Section 4 develops LKPBH in a way that makes it easily comparable with the approximations used in the EKPH method; it leads to an 8-Band Hamiltonian matrix. Section 5 evaluates the time consumed by calculations based on both methods. Finally some conclusions are drawn.

2. Theoretical background

K·P methods are based on developing a one-electron Hamiltonian into an orthonormal basis $|0,v,k\rangle = u_{0,v}\exp(i\boldsymbol{k}\cdot\boldsymbol{r})/\sqrt{\Omega}$ where $u_{0,v}(\boldsymbol{r})$ is a Γ-point Bloch function (GBF), which has the periodicity of the lattice, v is the band index, $\boldsymbol{k}$ is an arbitrary wavevector of the first Brillouin zone and Ω is the volume of calculation, which is large with respect to the nanostructure under study. The 0 index refers to the Γ point ($\boldsymbol{k}=0$). In this paper, we call this basis the standard basis. For zincblende semiconductors, it is very common to use an eight band renormalized matrix where the bands are the conduction band, (cb) and three valence bands (VBs): the heavy hole (hh), the light

hole (*lh*) and the spilt off (*so*) bands, each one double degenerated due to two different signs for the spin projection. This is the approach we will follow when using the LKPBH. The EKPH does not take the spin into account, and so considers only four bands.

The introduction of a nanostructure of a new material embedded in the host material induces an offset of the CB and VB edges. These usually form confining potentials for the CB and VB states. This offset is the potential to be used in the so called effective mass equations

$$-\frac{\hbar^2}{2m^*}\nabla^2\Phi + E_{v,0}(\mathrm{r})\Phi = E\Phi \tag{1}$$

where m^* is the effective mass and $E_{v,0}(\boldsymbol{r})$ is the band edge variable with the position because of the band offset introduced by the nanostructure. The hole effective masses are negative and different for the different bands (*hh*, *lh*, and *so*). Due to the negative effective mass, a pedestal offset potential in the VBs has the same confining properties of a well in the CB. These equations are widely used by device physicists.

In this paper, the conduction band states are divided into two groups, those in the bandgap of the host material, which form the IB (the IB is formed of *cb* states) and those within the conduction band of the host material which are the properly-speaking conduction band (CB) states.

The utilization of the effective mass equations requires the use of the integral factorization rule, which states that [12]

$$\int_{\Omega} f(\mathrm{r})g(\mathrm{r})d^3r \cong \left(\int_{\Omega} f(\mathrm{r})d^3r\right)\left(\int_{\Omega_{cell}} g(\mathrm{r})\frac{d^3r}{\Omega_{cell}}\right) \tag{2}$$

where f is a slowly varying function with negligible variation within a crystal unit cell, and g is a function with the translational periodicity of the lattice. Ω_{cell} is the unit cell volume. If this is fulfilled for the so-called envelope functions Ψ_v and GBFs $u_{0,v}$ respectively, both used in the next equation, the one-electron eigenfunctions are

$$\Xi(\boldsymbol{r}) \cong \sum_{v} u_{0,v}(\boldsymbol{r})\Psi_v(\boldsymbol{r}) \tag{3}$$

For the case that at least one of the wavefunctions is confined, the photon absorption coefficient by QDs is given by [13]

$$\alpha^{max}_{\Xi\to\Xi'} = \alpha'_{\Xi\to\Xi'}E\delta(E_{line}-E) \quad \text{with} \quad \alpha'_{\Xi\to\Xi'} = \frac{2\pi^2e^2}{n_{ref}ch\varepsilon_0}\frac{|\langle\Xi|\mathrm{r}\cdot\boldsymbol{\varepsilon}|\Xi'\rangle|^2}{4ab}F_sN_l \tag{4}$$

where n_{ref} is the index of refraction of the material involved, $2a$ and $2b$ are the dimensions of the QD base, F_s is the coverage factor of each QD layer and N_l is the number of layers per unit length in the growth direction. E_{line} is the photon energy and $\boldsymbol{\varepsilon}$ is the polarization vector. The super index max means that the state in the upper level is empty of electrons and the state in the lower level is full of them. The fraction of full and empty states will be factors in the calculation of the absorptions. In some cases, an additional factor of 2 will appear if transitions between spin up states and spin down states are to be added.

If the integral factorization rule is fulfilled, the dipole element of matrix for photon induced transitions depends only on the envelopes, as follows [3]:

$$\langle\Xi|\boldsymbol{\varepsilon}\cdot\mathrm{r}|\Xi'\rangle \cong \sum_{v}\langle\Psi_v|\boldsymbol{\varepsilon}\cdot\mathrm{r}|\Psi'_v\rangle \tag{5}$$

It is to be stressed that this expression is only valid if, at least, one of the envelopes is bound and fades at the infinite. In this paper the wavefunctions corresponding to the initial and the final states are both bound.

3. The Empiric K· P Hamiltonian

Let us start with the case in which the spin is neglected (spin and strain effects will be considered later). The Hamiltonian development in the standard basis is [12]

$$\begin{aligned}
&\forall\ v = v';\quad (H_0)_{v,v,\boldsymbol{k}} \equiv \langle 0,\ v,\ \boldsymbol{k}|H|0,\ v,\ \boldsymbol{k}\rangle = E_{v,0} + \frac{\hbar^2k^2}{2m_0}\\
&\forall\ v \neq v';\quad (H_0)_{v,v',\boldsymbol{k}} \equiv \langle 0,\ v,\ \boldsymbol{k}|H|0,\ v',\ \boldsymbol{k}\rangle = \frac{\hbar\mathrm{k}\cdot\mathrm{P}_{v,v'}}{m_0}\\
&\mathrm{P}_{v,v'} \equiv -i\hbar\langle u_{v,0}|\nabla u_{v',0}\rangle
\end{aligned} \tag{6}$$

(≡ is used for the definition of a new symbol), with m_0 being the electron mass in vacuo. Different values of $\boldsymbol{k}$ could have been considered for the initial and final states, but these matrix elements are all zero. Therefore, (H_0) is a four dimensional matrix whose terms are functions of $\boldsymbol{k}$.

Let us assume for a moment a homogeneous material with a zincblende lattice. The zincblende lattice belongs to the T_d symmetry group. The *cb* GBF is called $|S\rangle$ and has a spherical symmetry (it is an *s* function). At $\boldsymbol{k}=0$, the three VBs are degenerate and are linear combinations of the three GBFs called $|X\rangle$, $|Y\rangle$ and $|Z\rangle$ with the symmetry of *x*, *y* and *z* (see, e.g. [12]) respectively (they are p-functions). These functions fulfill the following:

$$\langle S|-i\hbar\frac{\partial}{\partial x}|X\rangle = \langle S|-i\hbar\frac{\partial}{\partial y}|Y\rangle = \langle S|-i\hbar\frac{\partial}{\partial z}|Z\rangle \equiv P_0 \tag{7}$$

The rest of the $P_{v,v'}$ are zero. P_0 is often called the Kane matrix element. This, with the knowledge of the bandgap ($E_{cv,0}=E_g$ and $E_{hh,0}=E_{lh,0}=E_{so,0}=0$), allows the matrix (H_0) to be written in full (round brackets represent a matrix). All the elements are analytical functions of $\boldsymbol{k}$ and the eigenvectors and eigenvalues can also be written (using Mathematica©) as analytical functions of $\boldsymbol{k}$ (see [4]). The $\boldsymbol{k}$-function eigenvalues are the so-called dispersion functions.

The analytical value of the CB eigenvalue (the dispersion function) allows for an analytical expression of the CB effective mass. By equating it with the experimental effective mass, the value of P_0 can be obtained. It is given by the following expression:

$$P_0 = \sqrt{\frac{E_g}{2}m_0\left(\frac{m_0}{m^*_{cb}}-1\right)} \tag{8}$$

Unfortunately, two of the three VB eigenvalue $\boldsymbol{k}$-functions (dispersion functions) are not acceptable because they present positive effective masses. The main reason for it is that the spin–orbit coupling has been neglected. The EKPH approximation is based on building a new Hamiltonian matrix (H_{EKP}) in which the VB eigenvalues are parabolic dispersion functions obtained from setting the experimental values of the effective masses and their position at $\boldsymbol{k}=0$ ($E_{cv,0}\equiv E_g$, $E_{hh,0}=E_{lh,0}=0$, $E_{so,0}\equiv -\Delta$). That is,

$$\begin{aligned}
E_{cb}(k) &= E_g + \frac{\hbar^2k^2}{2m_{cb}}\\
E_{hh}(k) &= -\frac{\hbar^2k^2}{2m_{hh}}\\
E_{lh}(k) &= -\frac{\hbar^2k^2}{2m_{lh}}\\
E_{so}(k) &= -\Delta - \frac{\hbar^2k^2}{2m_{so}}
\end{aligned} \tag{9}$$

By their experimental origin, the Hamiltonian so formed includes a number of effects that are neglected in (H_0). In particular, it neglects the spin–orbit coupling and the strain effects caused by the insertion of the QDs.

Following the usual procedure of the perturbation theory in the first order approximation (although strictly speaking this is not a perturbation calculation), the eigenvectors are considered unchanged. The CB dispersion function is also unchanged because the calculation of P_0 assumes the empiric *cb* effective mass.

Any Hamiltonian can be diagonalized by the transformation $(H_{0,d})=(D)(H_0)(D^+)$ where the rows of (D) are the eigenvectors of (H_0), normalized to unity. (D^+) is the Hermitian conjugate (the transpose of the complex conjugate) of (D). It is also its inverse, revealing that (D) is a unitary matrix. The diagonal elements of $(H_{0,d})$ are the calculated dispersion curves (eigenvalues) of (H_0), which are different to the empiric ones in Eq. (9).

When the empiric dispersion curves of all the bands are adopted as the new eigenvalues, the diagonal matrix $(H_{EKP,d})$ can be written straightforwardly. The matrix in the standard basis is then $(H_{EKP})=(D^+)(H_{EKP,d})(D)$.

The QD's shape is best approximated by a squat truncated quadrangular pyramid [14], but other shapes have also been considered in theoretical works, such as a lens [15] or a parallelepiped [16]. We also consider it as a parallelepiped or box of square basis ($a=b$) and short height c.

In general, the offset energy is position-dependent and different for each band (*cb, hh, lh* and *so*) as shown in Fig. 1. We show in this figure an accurate calculation [17] for an InAs QD of (non-truncated) pyramidal shape inside a matrix of GaAs. The potential is close with the square approximation often used, usually the same for the *hh* and *lh* bands. The *so* band is too low to be of interest.

The adoption of square potential wells or pedestals makes the calculations much easier. In this case, the effective-mass Eq. (1) can be solved for each band. An approximate calculation may consider the equation separable rendering the solutions $\Phi(r)$, the product of one-dimensional Schrödinger equations, which are very easy to solve. Their calculation for the case of confined functions is a harmonic function (cos or sin) in the center flanked by fading exponentials. The accuracy of the separable solutions has been thoroughly discussed [18]. The full energy spectrum for confined states of InAs QDs in GaAs is presented in Fig. 2. The quantum numbers representing the states correspond to the increasing values of the energy for each solution of the one-dimensional Schrödinger equation.

The separable approximation has been used in Fig. 2. An exact solution (within the square potential box approximation) leads to negligible changes for the IB states (those within the host bandgap) but reduction of about 52% for the most energetic states in the CB (the energy 0.9176 eV of the *cb* state $|cb442\rangle$ becomes 0.4070 eV), this reduction becoming increasingly smaller when approaching to the CB bottom. Errors are smaller in the VBs. The *hh*-levels are very close together and form a quasi-continuum that

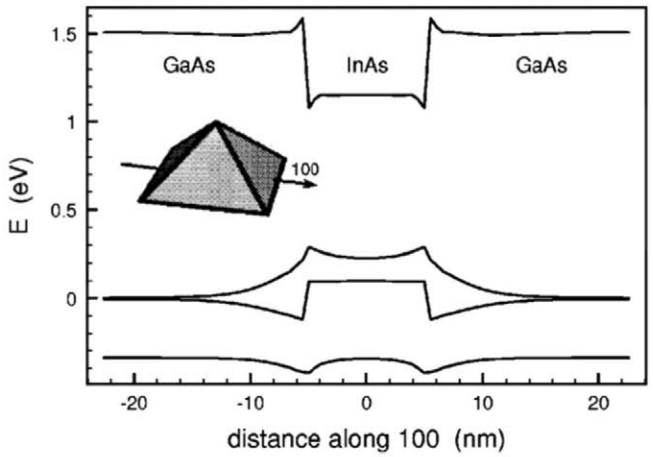

Fig. 1. Band structure based on the local value of the strain. Bands along the 100 direction, through the base of the QD. Reproduced with permission from APS 1998 [17].

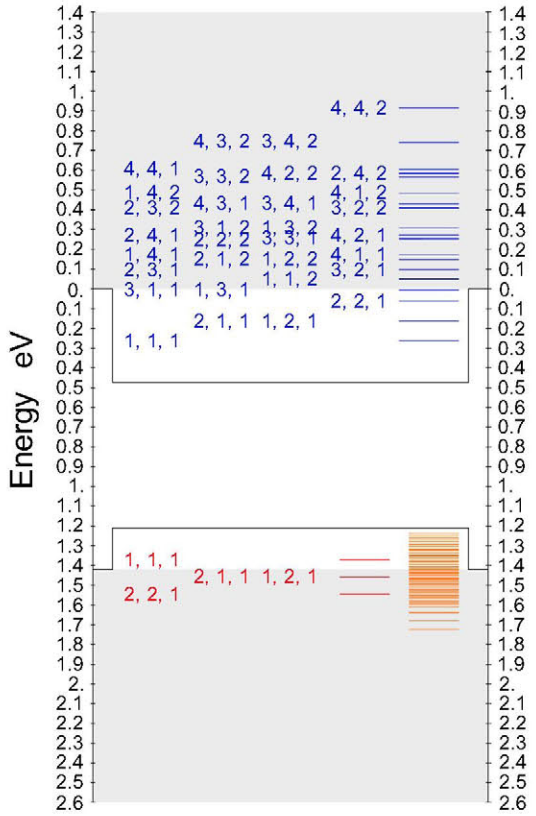

Fig. 2. Full energy spectrum for confined states in a InAs QD material in GaAs. Blue lines, *cb* states; red lines, *lh* states, orange lines, *hh* states; QD size: $2a=2b=16$ nm, $2c=6$ nm; CB offset, -0.473 eV; VB offset, 0.210 eV; effective masses (normalized to the electron mass in vacuo): *cb*, 0.0294; *hh*, 0.333; *lh*, 0.027. (For interpretation of the references to color in this figure legend, the reader is referred to the web version of this article.)

extends into the host VB. They do not leave space in the figure to write their quantum numbers.

Notice that some of the confined states are inside the CB or the VB of the host semiconductor. These states are called virtual bound states. They are degenerate with many extended states and play a very important role in the sub-bandgap photon-assisted transitions.

For the calculation of the envelope functions Ψ_S, Ψ_X, Ψ_Y and Ψ_Z, the following three steps are to be followed: (a) to obtain the discrete Fourier transform of the solution $\Phi(\boldsymbol{r})$ (this is a plane wave development); (b) to multiply by the appropriate element of the (D^+) matrix; and (c) to obtain the inverse discrete Fourier transform. The discrete Fourier transform of Φ is the solution of the Fourier Transform of the Schrödinger equation solution corresponding to a certain eigenenergy in a certain band. In the general case, which is not stationary, wavefunctions may have a component in each band and so form a column vector of four $\boldsymbol{k}$-dependent functions, but this is not an eigenfunction. The eigenfunction vector has a single non-zero term depending on the band the solution belongs to. When multiplied by (D^+), it is developed as a vector in the standard basis. Its inverse Fourier transform yields the four envelope functions to be used in Eq. (3).

Once the envelope functions are calculated, the optical matrix element is calculated as

$$\langle \Xi|\boldsymbol{e}\cdot\boldsymbol{r}|\Xi'\rangle \cong \langle \Psi_S|\boldsymbol{e}\cdot\boldsymbol{r}|\Psi'_S\rangle + \langle \Psi_X|\boldsymbol{e}\cdot\boldsymbol{r}|\Psi'_X\rangle + \langle \Psi_Y|\boldsymbol{e}\cdot\boldsymbol{r}|\Psi'_Y\rangle + \langle \Psi_Z|\boldsymbol{e}\cdot\boldsymbol{r}|\Psi'_Z\rangle \quad (10)$$

and the absorption coefficient for any transition is calculated with Eq. (4). The use of Eq. (10) requires that the integral factorization rule is fulfilled.

The *hh* confined states are so close that they form a quasi-continuum, which is in thermal contact with the VB. The *lh* states, which are in the same range of energies, are also embedded in this quasi-continuum. Therefore, it is usually assumed that they all are in thermal equilibrium with the VB and characterized by a single quasi-Fermi level: that of the VB. The transitions between each confined state of this enlarged VB and the IB states appear at energies below the host bandgap. Also, some *hh* or *lh* transitions to virtual bound states at the conduction band occur at energies below the host bandgap. Many of these transitions appear as an external current and form the sub-bandgap quantum efficiency of the IB solar cell. Transitions between extended states inside the host VB and the IB states occur also at sub-bandgap energies but their influence is very small [19].

To achieve sub-bandgap quantum efficiency, the transitions from the VB to the IB have to be completed with transitions between the IB and the CB. The strongest of these are the transitions whose final state is a virtual bound state in the CB. At room temperature, these transitions take place easily through thermal escape mechanisms with absorption of thermal photons or phonons.

We present in Fig. 3 the measured quantum efficiency (green solid line) and that calculated with the EKPH (blue dot-dashed line) for an exemplary solar cell (prototype SB in Ref. [20]). A reasonable, semi-quantitative, agreement is found. Other curves in the same figure are to be discussed later.

In the figure caption there is a mention to Givens rotations. The calculated dispersion functions of (H_0) are doubly degenerate for the *hh* and the *so* bands. In consequence, all the eigenvectors belonging to this degenerate space are valid and this implies that many diagonalization matrices (D) may be validly defined. A Givens rotation leaving the non-degenerate eigenstates [4] invariant fully defines (D). We select the (D)-matrix that better fits to the experimental quantum efficiency. Anyway any value of the Givens rotation between 0.0 and 0.5 [4] gives results which, not being the same, are semiquantitatively coincident with the experimental result and present reasonably well located first two peaks which are the only ones resolved in the experimental curve.

A pre-filling of the IB is made by introducing donor Si atoms in the IB region. When 20% of the QDs are prefilled, the absorption coefficient of Eq. (4) must be multiplied by 0.8 which is the fraction of empty states, which are therefore able to receive an electron.

4. Introducing the spin–orbit interaction and the strain effect in the Hamiltonian

When the spin is taken into consideration, the GBFs are associated to a spin, up or down, respectively denoted by $|S\uparrow\rangle$, $|X\uparrow\rangle$... and $|S\downarrow\rangle$, $|X\downarrow\rangle$ ... The spinors associated to these states have null in the lower or upper element. The (H_0) matrix is now an eight-dimensional matrix formed of two diagonal blocks of four-dimension submatrices, $(H_{0,\uparrow\uparrow})$ and $(H_{0,\downarrow\downarrow})$, both being identical.

The spin orbit interaction H_{so} is added to H_0. In the standard basis, for semiconductors with the zincblende lattice, (H_{so}) has the following non-null elements (the rest are null) [12],

$$\begin{aligned}&\langle X\uparrow|(H_{so})|Z\downarrow\rangle = -\langle X\uparrow|(H_{so})|Z\downarrow\rangle=\\ &i\langle Y\uparrow|(H_{so})|Z\downarrow\rangle = i\langle Y\uparrow|(H_{so})|Z\downarrow\rangle=\\ &i\langle X\uparrow|(H_{so})|Y\uparrow\rangle = -i\langle X\downarrow|(H_{so})|Y\downarrow\rangle = \Delta/3\end{aligned} \tag{11}$$

Δ is a constant to be obtained experimentally (already present in Eq. (9)). The full Hamiltonian matrix, which is eight dimensional, is not formed any more of two four dimensional diagonal blocks. For $\boldsymbol{k}=0$ the eigenvalues and the eigenstates are [12]

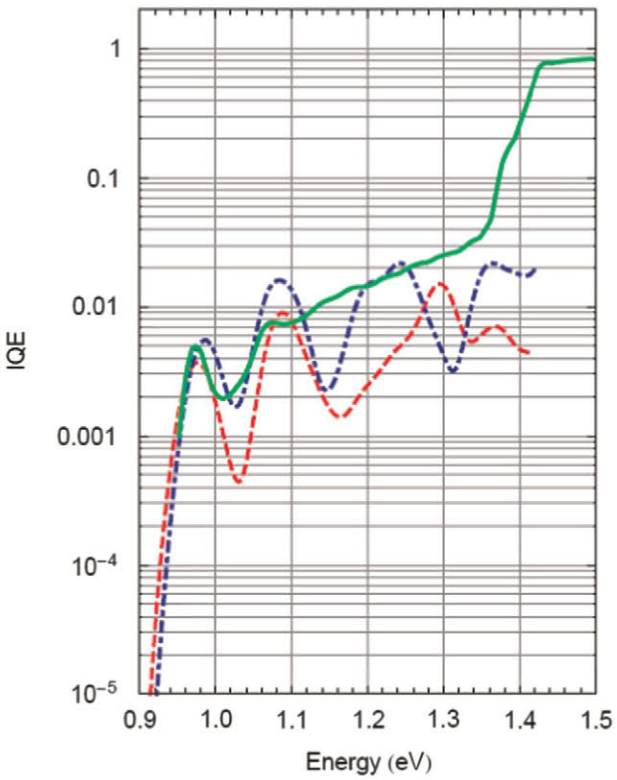

Fig. 3. Measured Internal Quantum Efficiency (IQE) of the exemplary cell (green solid line) as compared with the EKPH calculation (taken form [4]) for 0.2 Givens rotation (blue, dot-dashed line) and the eight band LKPBH calculation (red dashed line). In all the calculations, the fundamental IB is assumed prefilled to 20% with doping. (For interpretation of the references to color in this figure legend, the reader is referred to the web version of this article.)

Eigenvalue	Eigenstate
$E_{cb,0}$	$\|cb+\rangle = \|S\uparrow\rangle$
$E_{cb,0}$	$\|cb-\rangle = \|S\downarrow\rangle$
$E'_{VB,0} + \Delta/3 = E_{VB,0}$	$\|hh+\rangle = \frac{1}{\sqrt{2}}\|X\uparrow\rangle + \frac{i}{\sqrt{2}}\|Y\uparrow\rangle$
$E'_{VB,0} + \Delta/3 = E_{VB,0}$	$\|hh-\rangle = \frac{i}{\sqrt{2}}\|X\downarrow\rangle + \frac{1}{\sqrt{2}}\|Y\downarrow\rangle$
$E'_{VB,0} + \Delta/3 = E_{VB,0}$	$\|lh+\rangle = \frac{i}{\sqrt{6}}\|X\downarrow\rangle - \frac{1}{\sqrt{6}}\|Y\downarrow\rangle - i\sqrt{\frac{2}{3}}\|Z\uparrow\rangle$
$E'_{VB,0} + \Delta/3 = E_{VB,0}$	$\|lh-\rangle = \frac{1}{\sqrt{6}}\|X\uparrow\rangle - \frac{i}{\sqrt{6}}\|Y\uparrow\rangle + \sqrt{\frac{2}{3}}\|Z\downarrow\rangle$
$E'_{VB,0} - 2\Delta/3 = E_{VB,0} - \Delta$	$\|so+\rangle = \frac{1}{\sqrt{3}}\|X\uparrow\rangle + \frac{i}{\sqrt{3}}\|Y\downarrow\rangle + \frac{1}{\sqrt{3}}\|Z\uparrow\rangle$
$E'_{VB,0} - 2\Delta/3 = E_{VB,0} - \Delta$	$\|so-\rangle = -\frac{i}{\sqrt{3}}\|X\uparrow\rangle - \frac{1}{\sqrt{3}}\|Y\uparrow\rangle + \frac{i}{\sqrt{3}}\|Z\downarrow\rangle$

(12)

$E'_{VB,0}$ is the VB top in the absence of spin orbit coupling. With the coupling, its position is increased; it is the one actually measured. The split-off band is now pulled down by an amount Δ below the observed VB top. The eigenfunctions $|cb+\rangle$, $|cb-\rangle$, $|hh+\rangle$... are now the eight $u_{v,0}$ GBF used in Eq. (3). It is frequent that these eigenfunctions are denoted in relation with their group transformations. We prefer to use a more device-associated nomenclature in this paper.

The aspect of the matrix representing the Hamiltonian depends on the order we select the basis elements (although the change of order produces *identical* matrices), that is the GBFs. By ordering the basis' elements as $|cb+\rangle, |hh+\rangle, |lh+\rangle, |so+\rangle, |cb-\rangle, |hh-\rangle, |lh-\rangle, |so-\rangle$, the eight-dimensional matrix may be divided into four blocks,

$$(H) = \begin{pmatrix} (H_{uu}) & (H_{ul}) \\ (H_{lu}) & (H_{ll}) \end{pmatrix} \tag{13}$$

The interesting aspect of this block separation is that $(H_{lu}) = (H_{ul})^+$(Hermitian conjugate) and $(H_{ll}) = (H_{uu})^*$(complex conjugate); therefore, only two of the four matrices have to be determined. Other advantages will be explained later.

Each one of the block matrices may consider the sum of a kinetic matrix (the LK part), that applies to non-strained materials, and a strained material matrix (the PB part). Auxiliary functions are defined to write the matrix elements.

4.1. The Luttinger Kohn-Hamiltonian

For the LK part (the kinetic part) the auxiliary functions are [21]

$$\begin{aligned} O_{LK} &= \gamma_{cb}\frac{\hbar^2}{2m_0}\left(k_x^2 + k_y^2 + k_z^2\right) \\ Q_{LK} &= \gamma_2\frac{\hbar^2}{2m_0}\left(k_x^2 + k_y^2 - 2k_z^2\right) \\ R_{LH} &= \sqrt{3}\frac{\hbar^2}{2m_0}\left[\gamma_2\left(k_x^2 + k_y^2\right) - 2i\gamma_3 k_x k_y\right] \\ S_{LK} &= \sqrt{6}\frac{\hbar^2}{2m_0}\gamma_3(k_x - ik_y)k_z \\ T_{LK} &= \frac{\hbar P_0}{2m_0}(k_x + ik_y)/\sqrt{6} \\ U_{LK} &= \frac{\hbar P_0}{2m_0}k_z/\sqrt{3} \end{aligned} \tag{14}$$

where γ_{cb}, γ_1, γ_2, and γ_3 are the modified (see [21]) Luttinger parameters. Many of these parameters can be found in the literature [22].

The parameter $B = h\hbar P_0/m_0 d$, where d is an arbitrary normalizing constant, taken in this paper as 1 nm, is included in Table 1 calculated with the empiric values of P_0 given [17] for the InAs material. However, its value is slightly different from the one obtained using Eq. (8), which is 0.751. The values of B used in the calculations and appearing in Table 1 are obtained by fitting the effective masses in Appendix B, as described later.

The LK upper matrix block elements can now be written as

$$\left(H_{LK,uu}(\boldsymbol{k})\right) = \begin{pmatrix} E_{cb,0} + O_k & -\sqrt{3}T_{LK} & \sqrt{2}U_{LK} & -U_{LK} \\ -\sqrt{3}T_{LK}^* & E_{vb,0} - P_{LK} - Q_{LK} & \sqrt{2}S_{LK} & -S_{LK} \\ \sqrt{2}U_{LK}^* & \sqrt{2}S_{LK}^* & E_{vb,o} - P_{LK} + Q_{LK} & -\sqrt{2}Q_{LK} \\ -U_{LK}^* & -S_{LK}^* & -\sqrt{2}Q_{LK}^* & E_{vb,o} - P_{LK} - \Delta \end{pmatrix} \tag{15}$$

The asterisks refer to complex conjugates. No energy origin is assumed in this matrix. Actually, the band edges will be permitted to vary in the QD and in the barrier material. In certain calculations, it may be simplifying to put the energy origin in the valence band edge, so leading to $E_{cb,0}=E_g$ and $E_{vb,0}=0$.

Table 1
Initial inputs calculated with the InAs material parameters [17] (γ_{cb} is from [21]) and values obtained by fitting.

Parameter	Initial inputs: 8 bands	8 B unstrained fitting	8 B strained fitting
γ_{cb}	−1.202	0.75	−11.2
γ_1	6.084	3.5	3.5
γ_2	1.577	0.53	0.53
γ_3	2.497	0.53	0.53
χ_s		0	0.239
B (eV) @ $d=1$ nm	0.920	0.920	1.25
a_c (eV)	−6.66	–	−6.66
a_v (eV)	0.66	–	0.66
b_v (eV)	−1.		8–0.0091
d_v (eV)	−3.6	–	−3.6
E_g (eV)	0.418	–	–
Δ (eV)	0.38	–	–
l_{GaAs} (nm)	0.60583	–	–
l_{InAs} (nm)	0.56532	–	–

The non-diagonal matrix block $(H_{LK,ul})$ is

$$\left(H_{LK,ul}(\boldsymbol{k})\right) = \begin{pmatrix} 0 & 0 & -T_{LK}^* & -\sqrt{2}T_{LK} \\ 0 & 0 & R_{LK} & -\sqrt{2}R_{LK} \\ T_{LK}^* & R_{LK} & 0 & \sqrt{3}S_{LK} \\ -U_{LK}^* & -S_{LK}^* & -\sqrt{3}S_{LK} & 0 \end{pmatrix} \tag{16}$$

At the Γ-point ($\boldsymbol{k}=0$), the non-diagonal blocks are (0) and the diagonal blocks are diagonal matrices, each with the eigenvalues E_g, 0, 0 and $-\Delta$, if the origin of energy is located at $E_{VB,0}$. They can be taken from the column of initial values for non-strained material in Table 1.

When $\boldsymbol{k}\neq 0$, most of the zero elements disappear. The dispersion curves relating the eigenvalues with $\boldsymbol{k}$ (each one doubly degenerate) are represented in Fig. 4 for the 8-band Hamiltonian, numerically calculated with Mathematica©. Spherical symmetry (isotropy), simpler for calculations, is only approximately reproduced by the LK model (as expected from the non-isotropic space, structured as the zincblende) although the direction differences are small and not appreciated by many of the experiments.

This drawing seems to reveal that the dispersion curve isotropy is reasonably good.

The effective masses implied by these dispersion curves reveal positive effective mass in the conduction band and negative ones in the valence bands. Assuming a parabolic shape, they can be approximately calculated by

$$\frac{m^*}{m_0} = \frac{\hbar^2 k^2}{2m_0(E(k) - E(0))} \tag{17}$$

the effective mass being independent, in the strictly parabolic case, of the value of $\boldsymbol{k}$. In our calculations, $\boldsymbol{k}$ is taken as 0.1 nm^{-1}. Table 2 shows the effective masses calculated (as in [21]) for the different directions and the experimental values for the unstrained InAs [23]. We consider that they replicate the experimental data reasonably well (see e.g. [24] for details about the experimental methods) for the conduction and light-hole bands. However, based on the calculation of the effective mass (more sensible than the observation of Fig. 4), the calculated heavy-hole effective mass departs from isotropy sensibly and the split-off band is far from the reported measurement.

The excessive value of the hole effective mass in the (1,1,1) direction advices a parameter fitting. This fitting must affect only the parameters not associated with the strain. It is presented in Appendix A. The fitting results appear in Table 1, "8 B unstrained

fitting" column. The fitted effective masses appear in Table 2, "8-Band fitted parameters" column. A very good agreement between fitted and experimental effective masses is observed for all the directions analyzed. Nevertheless, this does not mean perfect isotropy. In other directions the agreement may be worse, forming the so called wrapped angular distribution.

The only effective mass which is not fitted is m_{so}. As the eigenstates of this band are deep into the valence band, they do not produce subbandgap transitions. Therefore, less attention is paid to this band in this work.

4.2. The Pikus–Bir Hamiltonian for a strained lattice

The auxiliary functions for the PB part, corresponding to the strained material, are related to the deformation tensor.

$$\begin{bmatrix} \varepsilon_{xx} & \varepsilon_{xy} & \varepsilon_{xz} \\ \varepsilon_{yx} & \varepsilon_{yy} & \varepsilon_{yz} \\ \varepsilon_{zx} & \varepsilon_{zy} & \varepsilon_{zz} \end{bmatrix} \equiv \begin{bmatrix} \dfrac{\partial u_x}{\partial x} & \dfrac{1}{2}\left(\dfrac{\partial u_x}{\partial y}+\dfrac{\partial u_y}{\partial x}\right) & \dfrac{1}{2}\left(\dfrac{\partial u_x}{\partial z}+\dfrac{\partial u_z}{\partial x}\right) \\ \dfrac{1}{2}\left(\dfrac{\partial u_y}{\partial x}+\dfrac{\partial u_x}{\partial y}\right) & \dfrac{\partial u_y}{\partial y} & \dfrac{1}{2}\left(\dfrac{\partial u_y}{\partial z}+\dfrac{\partial u_z}{\partial y}\right) \\ \dfrac{1}{2}\left(\dfrac{\partial u_z}{\partial x}+\dfrac{\partial u_x}{\partial z}\right) & \dfrac{1}{2}\left(\dfrac{\partial u_z}{\partial y}+\dfrac{\partial u_y}{\partial z}\right) & \dfrac{\partial u_z}{\partial z} \end{bmatrix} \tag{18}$$

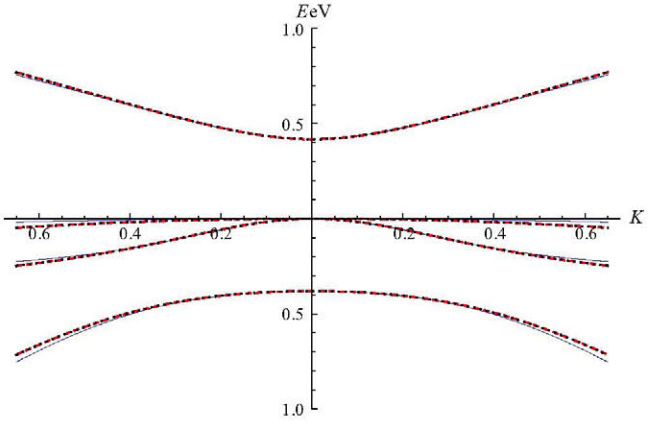

Fig. 4. Dispersion curves calculated following [21] in the (1,1,1) direction (solid line, blue), in the (1,0,0) or (0,1,0) directions (dashed line, red) and in the (0,0,1) direction (dotted line, black). Each line is doubly degenerate for the + and – eigenfunctions. The set of curves from up to down correspond to the *cb*, the *hh* the *lh* and the *so* bands. K is $\boldsymbol{k}$ in $\mathrm{nm}^{-1}|cb111\rangle$ state is assumed prefilled to 20% with doping. (For interpretation of the references to color in this figure legend, the reader is referred to the web version of this article.)

where u is the displacement of the points (e.g. the atoms' nuclei) with respect to their positions of equilibrium.

The auxiliary functions are

$$\begin{aligned} O_{PB} &= a_c(\varepsilon_{xx}+\varepsilon_{yy}+\varepsilon_{zz}) \\ P_{PB} &= -a_v(\varepsilon_{xx}+\varepsilon_{yy}+\varepsilon_{zz}) \\ Q_{PB} &= -b_v(\varepsilon_{xx}+\varepsilon_{yy}+\varepsilon_{zz}) \\ R_{PB} &= -\frac{\sqrt{3}}{2}b_v(\varepsilon_{xx}-\varepsilon_{yy})+id_v\varepsilon_{xy} \\ S_{PB} &= -\frac{d_v}{\sqrt{2}}(\varepsilon_{zx}-i\varepsilon_{yz}) \\ T_{PB} &= \frac{\hbar P_0}{2m_0}\big[(\varepsilon_{xx}+i\varepsilon_{yx})k_x+(\varepsilon_{xy}+i\varepsilon_{yy})k_y+(\varepsilon_{xz}+i\varepsilon_{yz}) \\ &\quad k_z\big]/\sqrt{6} \\ U_{PB} &= \frac{\hbar P_0}{2m_0}(\varepsilon_{zx}k_x+\varepsilon_{zy}k_y+\varepsilon_{zz}k_z)/\sqrt{3} \end{aligned} \tag{19}$$

and the upper Pikus–Bir diagonal block is

$$\left(H_{PB,uu}(\boldsymbol{k})\right)=\begin{pmatrix} O_{PB} & -\sqrt{3}T_{PB} & \sqrt{2}U_{PB} & -U_{PB} \\ -\sqrt{3}T_{PB}^* & -P_{PB}-Q_{PB} & \sqrt{2}S_{PB} & -S_{PB} \\ \sqrt{2}U_{PB}^* & \sqrt{2}S_{PB}^* & -P_{PB}+Q_{PB} & -\sqrt{2}Q_{PB} \\ -U_{PB}^* & -S_{PB}^* & -\sqrt{2}Q_{PB}^* & -P_{PB} \end{pmatrix} \tag{20}$$

The non-diagonal blocks are like in Eq. (16), but with the subindex PB.

4.2.1. A simple strain assumption for the quantum dot material

The introduction of a nanostructure in a host of different lattice parameter leads to a deformation of both materials. The displacements of the atoms can be calculated by minimizing the elastic energy. For this, the elastic 4-rank tensor is to be known for the materials involved. Using the displacements in a lattice of calculation points as variables, their positions are calculated to obtain the minimum [25].

The deformations affect significantly the electronic variables. Energy eigenvalues and eigenstates are modified. The electronic energy may be subsequently introduced in the minimization process. In any case, the deformations vary with the position and, consequently, so do the band edges, affecting the offset potentials, as shown in Fig. 1, which in the EKPH are usually taken as square for simplicity. These squared potentials are only possible if very simple deformation tensors are used. Consequently, we assume that the host material is not deformed and that the QD material tends to adopt, in a first instance, the lattice parameters of the host material. Under these conditions, taking the coordinate origin to be in the center of the QD box, the displacements are

Table 2
Effective masses calculated for unstrained material (data in Table 1, initial inputs column) for the 8B models of the references, and the experimental values.

Eff. mass	Tomic et al. [21]			8-Band fitted parameters			Experimental unstrained [23]
Direction	(1,1,1)	(1,0,0)	(0,0,1)	(1,1,1)	(1,0,0)	(0,0,1)	Any
m_{cb}	0.023	0.023	0.023	0.023	0.023	0.023	0.023
m_{hh}	−0.917	−0.341	−0.341	−0.410	−0.410	−0.410	−0.41
m_{lh}	−0.023	−0.024	−0.024	−0.026	−0.026	−0.026	−0.026
m_{so}	−0.064	−0.064	−0.064	−0.077	−0.077	−0.077	−0.16

$$u_x(\boldsymbol{r}) = \chi_s x\left(\frac{l_{GaAs}}{l_{InAs}} - 1\right)$$
$$u_y(\boldsymbol{r}) = \chi_s y\left(\frac{l_{GaAs}}{l_{InAs}} - 1\right)$$
$$u_z(\boldsymbol{r}) = \chi_s z\left(\frac{l_{GaAs}}{l_{InAs}} - 1\right) \tag{21}$$

where χ_s is a fitting parameter that is one if the QD material takes strictly the lattice constant of the host. The lattice constants in this equation (l_c) may be found in Table 1.

By application of Eq. (17), the deformation tensor elements are

$$\varepsilon_{xx} = \varepsilon_{yy} = \varepsilon_{zz} = \chi_s\left(\frac{l_{GaAs}}{l_{InAs}} - 1\right)$$
$$\varepsilon_{xy} = \varepsilon_{yz} = \varepsilon_{zx} = \varepsilon_{yx} = \varepsilon_{zy} = \varepsilon_{xz} = 0 \tag{22}$$

In reality, the host lattice constant is also modified and strong shear stresses appear in the edges. In all, the potential is not squared; it has peaks in the edges and extends outside the QD (Fig. 1). However for the sake of simplicity we have neglected these complexities and adopted square potentials in the EKPH approximation and we shall do the same with the LKPBH approximation, because the purpose of this work is to compare both approximations in the same conditions. However, other choices of the deformation tensor elements may lead to square potentials. We believe that the choice of the strain model is not so important as far as the parameter fitting in Appendix B, to be explained later, leads to a good fit of the band positions and of the effective masses.

At the Γ point, the non-diagonal bloc matrices are zero so that the 8-band Hamiltonian has the same energy eigenvalues as the upper diagonal matrix, although doubly degenerated. With the strain model described above, the eigenvalue corresponding to the CB bottom is given by

$$E_{CB} = E_g + \left(\frac{l_{GaAs}}{l_{InAs}} - 1\right)a_c(InAs)\chi_s \tag{23}$$

whereas E_{VB} is about 10 meV. Thus we can adopt for E_{CB} the experimental bandgap in the strained QD used in the EKPH approximation, which is 0.734 eV [3]. By taking the parameter values in Table 1 (E_g is the unstrained QD material), χ_s=0.238772.

Notice that the host and QD-material lattice constants and the unstrained QD-material bandgap are considered very well known.

4.2.2. Eight band effective mass fitting in the strained material

The rough approximation adopted for the strain model requires a fitting of the strain-associated parameters. For the strained material, the experimental bandgap is rather different form the bulk InAs, as shown in Table 3 ("EKPH" column). Also, the effective masses are somewhat different. Details of the fitting procedure are given in Appendix B.

The fitting values are reported in Table 1 and the resulting effective masses are shown in Table 3. It can be observed that the isotropy is, in general, very good, especially for the m_{cb}, the m_{so} and the m_{lh}; it is less good for the m_{hh}; the non-fitted m_{so} is not far from the experimental value.

4.3. Energy spectrum and envelope functions in the eight band Luttinger–Kohn–Pikus–Bir Hamiltonian

4.3.1. The energy spectrum

The QD material, with the simplified strain described above caused by its inclusion in the host material, presents parabolic dispersion functions for low values of $\boldsymbol{k}$ with the effective masses in Table 3, column "8-B strained & fitted". With the exception of the *hh* band the effective masses are closely isotropic and reach values similar to those attributed to the effective masses in reference [4] for the EKPH. For simplicity we must admit isotropy also for the *hh* band effective mass, with the value in the (1,1,1) direction. The diagonalized Hamiltonian matrix, denoted as ($H_{LKPB,d}$), has the parabolic dispersion functions ruled by the isotropic effective masses. Schrödinger effective mass equations can then be formulated, as in the EKPH case, with the same band effective masses; although in this case the equations are eight forming four couples of equations with two exactly equal equations in each couple. Therefore, the functions Φ acting as eigenfunctions are the same as those in the EKPH case. Since the band offsets are also the same (see Table 3, "8B-strained & fitted" and "EKPH" columns), the energy spectra are also exactly the same, with each value doubly degenerate. The energy spectra are represented in Fig. 2 for the exemplary InAs/GaAs solar cell.

Summarizing, with the simplified strain adopted and the assumption of isotropy, the EKPH and the LKPBH have the same energy spectra.

4.3.2. The envelope functions

Once the Φ eigenfunctions are known, the procedure for obtaining the envelope functions is the same as the one described in steps (a)–(c) in Section 3. However, the diagonalizing matrix formed by the eigenvectors, now denoted as (D^{+}_{LKPB}) is different from (D^{+}) used in the EKPH method. It is formed of the eigenvector components of (H_{LKPB}) and not of those of (H_0). As the matrix now has eight dimensions, they have to be calculated numerically (algebraic equations of the 8th order do not have analytic solutions with generality) for each value of $\boldsymbol{k}$ to be used in the discrete Fourier Transforms.

The electron eigenfunction is formed with these envelopes applying Eq. (3) with eight summands in this case. The GBF are$|cb+\rangle$, $|hh+\rangle$, $|lh+\rangle$, $|so+\rangle$, $|cb-\rangle$, $|hh-\rangle$, $|lh-\rangle$and $|so-\rangle$. The envelopes may be labeled as, e.g. $\Psi^{(cb-,121)}_{|lh+\rangle}$, which means the envelope multiplying GBF $|lh+\rangle$ is derived from the Φ of band $(cb-)$, with quantum numbers (1,2,1). The superscript may be removed in some generic formulas.

4.4. The absorption coefficients

The absorption coefficient is now calculated using Eq. (4). The matrix element appearing in this equation is now

$$\begin{aligned}\langle\Xi|\boldsymbol{\varepsilon}\cdot\boldsymbol{r}|\Xi'\rangle \cong{}& \left\langle\Psi_{|cb+\rangle}\middle|\boldsymbol{\varepsilon}\cdot\boldsymbol{r}\middle|\Psi'_{|cb+\rangle}\right\rangle + \left\langle\Psi_{|hh+\rangle}\middle|\boldsymbol{\varepsilon}\cdot\boldsymbol{r}\middle|\Psi'_{|hh+\rangle}\right\rangle \\ &+ \left\langle\Psi_{|lh+\rangle}\middle|\boldsymbol{\varepsilon}\cdot\boldsymbol{r}\middle|\Psi'_{|lh+\rangle}\right\rangle + \left\langle\Psi_{|so+\rangle}\middle|\boldsymbol{\varepsilon}\cdot\boldsymbol{r}\middle|\Psi'_{|so+\rangle}\right\rangle \\ &+\left\langle\Psi_{|cb-\rangle}\middle|\boldsymbol{\varepsilon}\cdot\boldsymbol{r}\middle|\Psi'_{|cb-\rangle}\right\rangle + \left\langle\Psi_{|hh-\rangle}\middle|\boldsymbol{\varepsilon}\cdot\boldsymbol{r}\middle|\Psi'_{|hh-\rangle}\right\rangle \\ &+ \left\langle\Psi_{|lh-\rangle}\middle|\boldsymbol{\varepsilon}\cdot\boldsymbol{r}\middle|\Psi'_{|lh-\rangle}\right\rangle + \left\langle\Psi_{|so-\rangle}\middle|\boldsymbol{\varepsilon}\cdot\boldsymbol{r}\middle|\Psi'_{|so-\rangle}\right\rangle\end{aligned} \tag{24}$$

Table 3
Band edges and effective masses with the parameters fitted in Table 1 and experimental values used in [4].

Band edges and relative effective masses	8B-strained and fitted			EKPH
E_c (eV)	0.737			0.737
E_{vhh} (eV)	−0.032			0
E_{vlh} (eV)	−0.031			0
E_{vso} (eV)	−0.412			−0.212
Direction	(1,1,1)	(1,0,0)	(0,0,1)	Any
m_{cb}	0.0294	0.0293	0.0294	0.0294
m_{hh}	−0.333	−0.185	−0.246	−0.333
m_{lh}	−0.027	−0.029	−0.027	−0.027
m_{so}	−0.062	−0.062	−0.062	−0.076

The superscript has been removed for generality, but absorption is produced by transitions between a state of a given band and states of the eight bands (including states of the same band of the initial state, which are intraband transitions).

We show in Fig. 5 the sub-bandgap transitions between all the bound states in the VBs ($hh\pm$ and $lh\pm$ states; the $so\pm$ states fall outside this range) and the bound $cb\pm$ states (IB states and virtual bound states within the host CB). Each transition must be calculated separately and all of them must be summed up. Actually we have calculated all transitions of the VB states and a given *cb* state. These absorption coefficients are labeled as VB-xxx, xxx referring to the quantum numbers labeling the final *cb* state. More precisely the final state includes the $cb+$ and $cb-$ bands and if they are degenerate, like the 121 and 212 states, both are considered together (each one with the two spins). Finally, all these absorption coefficients are summed up together. Notice that, when summing up the absorption coefficients, the VB-111 coefficient is multiplied by 0.8 because in the exemplary cell 20% of the (1,1,1) states is supposed to be filled with electrons by doping. Similar curves appear in [4] (Fig. 6) concerning the EKPH.

With this absorption coefficient, and under the assumption that all the transitions are collected as external current, the internal quantum efficiency is calculated and drawn in Fig. 3 (red dashed curve) together with the measured curve and the curve calculated with the EKPH.

As explained for the EKPH, the appearance of a photocurrent through the IB states requires that there is a mean for performing the IB–CB transitions. It has been said that due to the small IB–CB gap this transition may be easily made with the help of thermal photons or phonons.

5. Discussion on the calculation time

The calculation of the envelope functions starts with the calculation of eigenfunctions of the TISE equation with the effective mass of the final state, which is *cb* state (it may be an IB or a virtual bound state). Since, for the case of a box-shaped QD with squared potential, the solution is analytic and well known, no time is needed for its determination (it is known beforehand). However the treatment used requires the numeric calculation of the eigenfunction in the nodes of the calculation lattice. This lattice, in our calculations, consists of $41\times41\times41$ cells each of $1.5\times1.5\times1.5\,\mathrm{nm}^3$. The total number of nodes for calculation is 68921. Nevertheless, the time for this calculation, for example, for a final state, is in the order of one second, using Mathematica 7 and a notebook (Core i5) for it. The same can be said for an initial state.

This calculation is followed by a calculation of the Discrete Fourier Transform in 68921 nodes of the final state and its multiplication by the diagonalization matrix element, which should have been calculated previously (as we see later, this time is counted apart). Then, the same is done for all the *hh* and *lh* initial states, of which there are in the range of 200. Finally, in the case of vertical illumination, the elements of matrix are calculated for the *x* and *y* polarizations. In the EKPH, the calculation of the set of matrix elements associated to a single final state takes about 5 min. In the LKPBH, the time for preceding calculations is multiplied by 2 because there are 8 envelopes instead of 4, that is, 10 min.

Finally, all the given final states are summed up to obtain the absorption coefficient of the transitions from the VB to this final state; this process may last about 3 min for the EKPH. With a typical total of 10 final states within the bandgap, the duration is about $(5+3)\times10=80$ min. For the LKPBH there is a factor of 8, due to the double number of envelopes in each transition times the double number of initial states in the VB times the double number of final states in the IB/CB, in both cases due to the spin degeneracy; thus the de duration for the LKPB Hamiltonian is 640 min. The calculation of the total absorption once the absorption to each final state has been calculated is negligible.

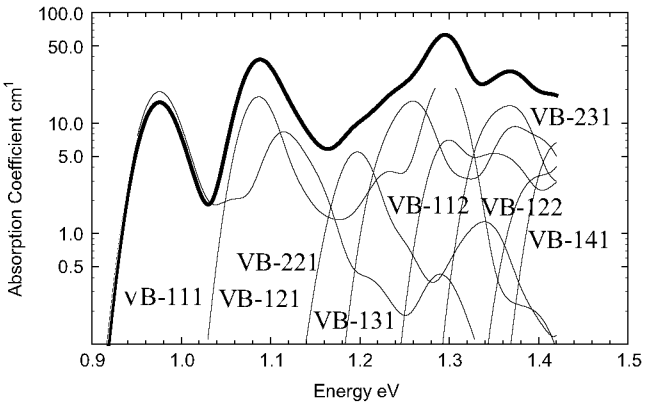

Fig. 5. Sub-bandgap absorption calculated with the eight band LKPB (thick black line) and contribution of the transitions from all the bound states in the *hh* and *lh* bands to the *cb* states (including the IB states). In the legends, each curve is labeled with the quantum numbers of the *cb* final state.

The calculation of the diagonalization elements of matrix in the 68,921 nodes (the time said before to be counted apart) is by far the most time-consuming factor. In the case of the EKPH model, each element of matrix is analytic and the calculation takes less than one minute. However, in the 8B LKPBH method, the eigenvalues must be calculated numerically for each one of the 68921 nodes. This takes about 200 min per element in the same machine. Assuming that calculations use the *lh* and the *hh* bands as initial states, and the *cb* band as final states, the matrix elements to be calculated are 12 (the 4 elements in the *cb*, the *lh* and the *hh* rows) for the EKPH method and 48 for the 8B LKPBH method (the 8 elements *cb*, the *lh* and the *hh* rows, each affected of plus and minus spins, that is in 6 rows); in total, $200\times4=800$ times more than in the EKPH.

By summing up all the before-indicated times, the calculation of the subbandgap absorption with the EKPH may last about $12+80=92$ min and with the LKPBH it may last $12\times800+640=10240$ min, that is, about $1\frac{1}{2}$ h for the EKPH and over 170 h for the LKPB Hamiltonian. We consider that the LKPB Hamiltonian does not fulfill the requirement of being adequate for device development with feedback of results, at least with the calculation methods used.

It is to be noted that the times indicated correspond to highly automated software. The software actually used requires frequent interaction with the operator and the times are substantially extended. Furthermore, these times are an estimate. Not all the calculations of similar nature last the same, and the number of states is an approximation.

6. Conclusions

Bands offsets are a concept frequently used. It is shown that, strictly speaking, constant band offsets are only possible if the strain corresponds to a hydrostatic pressure in the QDs. However, it is shown in the literature that they are a good simplifying approximation in many cases.

Under the same assumptions, of box-shaped QDs and constant band offsets, the energy spectrum is the same EKPH than in the theoretically well supported and widely used LKPBH. But we must warn the reader that the drastic approximations made into the LKPBH to compare it to the EKPH may lead to a spectrum somewhat different than the real one.

The absorption coefficients may be calculated with EKPH and with the LKPBH and they give results which are reasonably similar. This is also an asset for using the simpler EKPH.

The agreement between the measured internal quantum efficiency and the one calculated with the EKPH is better than when it is calculated with the LKPBH. At a first sight, this is surprising because the LKPBH is deemed to be more accurate than the EKPH. This accuracy is strongly destroyed by the rough strain model adopted in this paper and also by the inexactness of the assumption of isotropy for the *hh* effective mass. In contrast, the variety of diagonalization matrices (^{G}D) motivated by the degeneracy of the *hh* and *so* bands in the (H_0) matrix allows selecting the value of the Givens rotation that produces a best fitting with the measured internal quantum efficiency. However the fact that the diagonalization matrix (^{G}D) is fitted removes much of the predictive role of the EKPH method for determining aspects such as the best size of the QDs or other optimization characteristics. The LKPBH method, even with the simplifications made in this paper, is thought to better maintain this predictive nature.

As we have seen, the calculation of the sub-bandgap quantum efficiency of QD IB solar cells using the 8B LKPBH is about 100 times more time consuming than using the EKPH. Indeed, the 8B LKPBH is very adequate for accurate calculations provided that the dimensions and compositions of the QDs are properly set. This accuracy requires a better estimate of the field of strains and also powerful computing means, as it happens in all the papers on the topic that we have looked at.

In summary, the use of the EKPH is supported by similarities with the results obtained with the well established LKPBH and is much simpler to use.

Acknowledgments

This project has been supported by the Mega-grant 14B25.31.0020 from the Russian Ministry of Education and Science, the EC NGCPV (283798) grant and by the Spanish National Research Program PROMESA (ENE2012-37804-C02-01).

Appendix A. Effective mass fitting in the unstrained material in the eight band model

The use of the same value for γ_2 and γ_3 leads to the same value for the m_{hh} effective masses in all the directions in Table 2. This does not mean that perfect isotropy is achieved outside the directions studied; the curvature of the dispersion functions (effective mass) is different, but this choice provides a good pinning to avoid excessive anisotropy in m_{hh}.

Variations of γ_{cb} and γ_2 produce very minor modifications of all the effective masses in the (111) direction, although the former can be used for fine trimming of the m_{cb}. This is done as a first step of the fitting process and the result is in Table 1, "8 B unstrained fitting" column.

Fig. A1 shows the variation of all the effective masses with $\gamma_2=\gamma_3$ in the (111) direction. Since only m_{hh} is strongly variable, it can be adjusted leaving the rest of the effective masses unchanged.

A fine fitting of m_{lh} can be achieved by varying γ_1. This will not affect m_{cb} but will modify m_{hh} strongly. Therefore the fitting of m_{lh} and m_{hh} has to be done with γ_1 and $\gamma_2=\gamma_3$ simultaneously. The resulting parameters are in Table 1, "8 B unstrained fitting" column and the fitted effective masses appear in Table 2 ("8-Band fitted parameters" column).

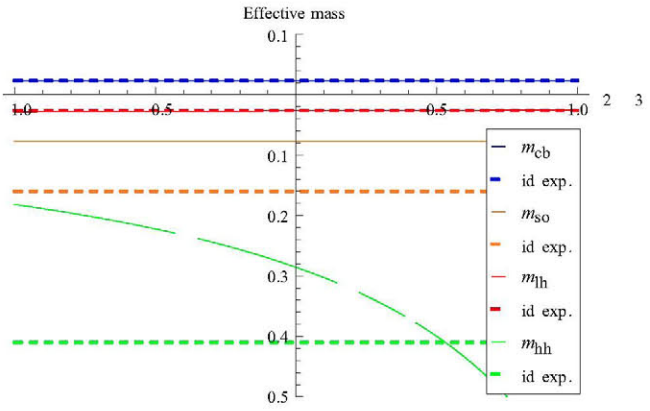

Fig. A1. Effective masses in the (1,1,1) direction vs. $\gamma_2=\gamma_3$ when the rest of the parameters are those in Table 1 (8-B unstrained fitting column). Solid lines are for the calculated effective mass and dashed lines show the corresponding experimental effective mass. The effective mass m_{hh} is fitted for $\gamma_2=\gamma_3=0.53$.

Appendix B. Effective mass fitting in the strained material in the eight band model

The calculations to be followed are made using the fitted parameters for the bulk material in Table 1, "8 B unstrained fitting" column.

Among the strain related parameters, the heavy-hole effective mass in the (1,1,1) direction can only be fitted by varying b_v(InAs). As shown in Fig. B1, the m_{cb} and m_{so} effective masses do not change and m_{lh} varies slightly. The fitting value is $b_v=-0.0092$ (to be changed in the final adjustment, as explained later).

If the bandgap fitting is to be kept, no fitting of the rest of the effective masses can be found by varying other strain parameters. We are led to revisit the kinetic parameters. γ_{cb} affects only the m_{cb} effective mass, but this effective mass is also affected by B for which different values have been found depending on the calculation method. The parameter γ_{cb} is considered to be dependent on a parameter to fit m_{cb} and is not primarily associated to the Luttinger parameters given in the literature: it is not a property of the unstrained material. The value of B is also subject to different estimates. A simultaneous variation of γ_{cb} and B allows for the simultaneous fitting of m_{cb} and m_{lh}. At the end (when m_{cb} and m_{lh} are fitted) b_v has to be adjusted again. The fitting values are reported in Table 1 and the resulting effective masses are in Table 3. It can be observed that the isotropy is, in general, very

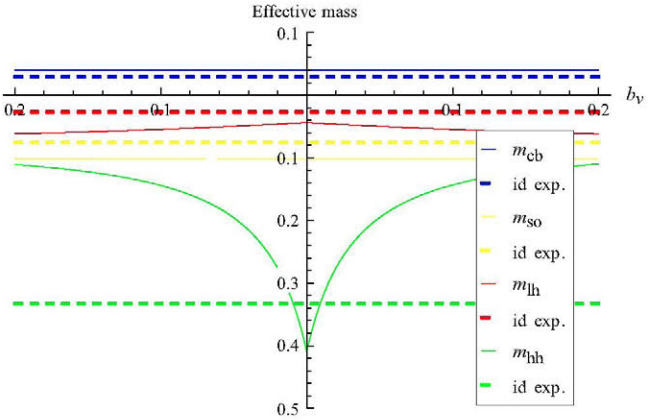

Fig. B1. Effective masses vs. b_v when the rest of the parameters are those in Table 1 "Initial inputs" column. Solid lines are for the calculated effective mass and dashed lines show the corresponding experimental effective mass. The effective mass m_{hh} is fitted for $b_v=-0.0092$.

good, especially for the m_{cb}, the m_{so} and the m_{lh}; it is less good for the m_{hh}; and the non-fitted m_{so} is not far from the experimental value.

References

[1] A. Luque, A. Martí, Increasing the efficiency of ideal solar cells by photon induced transitions at intermediate levels, Phys. Rev. Lett. 78 (1997) 5014–5017.
[2] A. Martí, L. Cuadra, A. Luque, Quantum dot intermediate band solar cell, in: Proceedings of the 28th IEEE Photovoltaics Specialists Conference, IEEE, New York, 2000, pp. 940–943.
[3] A. Luque, A. Marti, E. Antolín, P.G. Linares, I. Tobías, I. Ramiro, E. Hernandez, New Hamiltonian for a better understanding of the quantum dot intermediate band solar cells, Sol. Energy Mater. Sol. Cells 95 (2011) 2095–2101.
[4] A. Luque, A. Mellor, E. Antolin, P.G. Linares, I. Ramiro, I. Tobias, A. Marti, Symmetry considerations in the empirical K·P Hamiltonian for the study of intermediate band solar cells, Sol. Energy Mater. Sol. Cells 103 (2012) 171–183.
[5] J.M. Luttinger, Quantum theory of cyclotron resonance in semiconductors – general theory, Phys. Rev. 102 (1956) 1030–1041.
[6] W. Kohn, Shallow impurity states in silicon and germanium, Solid State Phys. – Adv. Res. Appl. 5 (1957) 257–320.
[7] G.E. Pikus, G.L. Bir, Effect of deformation on the energy spectrum and the electrical properties of imperfect germanium and silicon, Sov. Phys. – Solid State 1 (1959) 136–138.
[8] G.E. Pikus, G.L. Bir, Cyclotron and paramagnetic resonance in strained crystals, Phys. Rev. Lett. 6 (1961) 103–105.
[9] G. Dresselhaus, A.F. Kip, C. Kittel, Plasma resonance in crystals – observations and theory, Phys. Rev. 100 (1955) 618–625.
[10] E.O. Kane, Energy band structure in p-type germanium and silicon, J. Phys. Chem. Solids 1 (1956) 82–99.
[11] E.O. Kane, The K·P method, in: R.K. Willardson, A.C. Beer (Eds.), Physics of III–V Compounds, Academic, New York, 1966, pp. 75–100.
[12] S. Datta, Quantum Phenomena, Addison Wesley, Reading (MA), 1989.
[13] A. Messiah, Mécanique Quantique, Dunod, Paris, 1960.
[14] D. Bimberg, M. Grundmann, N.N. Ledentsov, Quantum Dot Hetrostructures, Wiley, England, 1999.
[15] V. Popescu, G. Bester, A. Zunger, Strain-induced localized states within the matrix continuum of self-assembled quantum dots, Appl. Phys. Lett. 95 (2009) 023108.
[16] O.L. Lazarenkova, A.A. Balandin, Miniband formation in a quantum dot crystal, J. Appl. Phys. 89 (2001) 5509–5515.
[17] C. Pryor, Eight-band calculations of strained InAs/GaAs quantum dots compared with one-, four-, and six-band approximations, Phys. Rev. B 57 (1998) 7190–7195.
[18] A. Luque, A. Mellor, I. Tobías, E. Antolín, P.G. Linares, I. Ramiro, A. Martí, Virtual-bound, filamentary and layered states in a box-shaped quantum dot of square potential form the exact numerical solution of the effective mass Schrödinger equation, Physica B 413 (2013) 73–81.
[19] A. Luque, A. Mellor, I. Ramiro, E. Antolín, I. Tobías, A. Martí, Interband absorption of photons by extended states in intermediate band solar cells, Sol. Energy Mater. Sol. Cells 115 (2013) 138–144.
[20] E. Antolín, A. Marti, C.D. Farmer, P.G. Linares, E. Hernández, A.M. Sánchez, T. Ben, S.I. Molina, C.R. Stanley, A. Luque, Reducing carrier escape in the InAs/GaAs quantum dot intermediate band solar cell, J. Appl. Phys. 108 (2010) 064513.
[21] S. Tomic, A.G. Sunderland, I.J. Bush, Parallel multi-band **k** center dot p code for electronic structure of zinc blend semiconductor quantum dots, J. Mater. Chem. 16 (2006) 1963–1972.
[22] I. Vurgaftman, J.R. Meyer, L.R. Ram-Mohan, Band parameters for III–V compound semiconductors and their alloys, J. Appl. Phys. 89 (2001) 5815–5875.
[23] InAs: Effective Masses and Density of States, Ioffe Institute Data Basis.
[24] K.W. Boer, Survey of Semiconductor Physics, Van Nostrand Reinhold, New York, 1990.
[25] C. Pryor, M.E. Pistol, L. Samuelson, Electronic structure of strained InP/$Ga_{0.51}In_{0.49}P$ quantum dots, Phys. Rev. B 56 (1997) 10404–10411.